

## Influence of Synthesis Route on the Structural and Optical Properties of a Potential Multifunctional Oxide: $Zn_{1-x}Sr_xO$

Shekhar D. Bhame\* and Rishi Prasad

*Symbiosis Institute of Technology, Symbiosis International (Deemed) University, Lavale, Pune, 412115, Maharashtra, India*

Received 28 October 2021; Accepted 29 December 2021

### Abstract

We report the synthesis of Sr doped ZnO ( $Zn_{1-x}Sr_xO$  with  $x=0, 0.01, 0.02, 0.03$  and  $0.04$ ) by three different methods to study the dependence of synthesis on the structural and optical properties. The study is a comparison of auto combustion, citrate gel and co-precipitation method derived oxide samples. A comparative analysis like this enabled us to identify the right method for doping Sr in the ZnO matrix with minimum additional reflections. Further analysis revealed the formation of defects in the crystal can act as potential phonon scattering centres for thermoelectric application. Absorption data reveal that, while auto combustion method led to excellent absorption in the visible light region, only 3% doped ZnO by citrate gel exhibited the same and was completely absent in the materials derived from traditional co-precipitation technique. Such absorption between 400 to 700 nm by just a mono doped binary oxide may lead to excellent photocatalytic dye degradation properties. Also, it was found that Burstein Moss shift and introduction of Sr-3d levels in conduction band can further enhance the electrical conductivity which again is a way to tune thermoelectric figure of merit. Hence studying such a simple binary oxide doped with Sr becomes important as it can be a very good multi multifunctional material.

*Keywords:* Sr doped ZnO, Synthesis route optimization, Multifunctional oxide

### 1. Introduction

The rising interest in wide bandgap semiconductors has led to immense research in ZnO based materials. ZnO possess a hexagonal wurtzite structure where the oxygen is surrounded by 4 zinc atoms at the corners of a tetrahedron or vice versa. Though it exhibits  $sp^3$  hybridization and covalent character, they are ionic [1]. ZnO has been studied for various applications such as uv-detectors, solar cell applications, photocatalysis, thermoelectric applications, sensing applications, biological applications and more [2-7]. Although there have been various reports of metal doped ZnO [8-14], Al doped ZnO have been widely studied for their thermoelectric and photocatalytic applications [15-22]. It is a well-known fact that the physiochemical properties of oxides, specially ZnO depends on the synthesis route. Extensive study on the effect of synthesis on the properties of ZnO can be found elsewhere [23-28]. Since such a dependence of the synthesis route was observed on the properties of ZnO, it becomes crucial to understand the influence of synthesis on the structural and optical properties on the doped system (i.e., Sr doped ZnO) as they have been gaining attention in the recent past. But such a study was not available in the literature for the Sr doped ZnO.

A higher ionic radii element like  $Sr^{2+}$  ( $1.18 \text{ \AA}$ ) when substituted with  $Zn^{2+}$  ( $0.74 \text{ \AA}$ ) ions in the ZnO matrix can lead to lattice defects. These defects have the potential to alter structural and optical property of the base compound. The defect enhanced introduction of intermediate energy levels have been studied previously by Sheetz *et al* [29]. Such introduction of fresh defect states has been previously

reported to exhibit visible light absorption and photoconductivity [30; 31]. The defects introduced due to the doping of  $Sr^{2+}$  can lead to visible light enhanced photocatalytic degradation. Since there are only a limited literature available for the use of Sr doped ZnO for photocatalytic studies, this composition would be a promising material to investigate. At the same time, the introduction of  $Sr^{2+}$  also has been reported to increase the electrical conductivity [32]. Electrical conductivity is directly related to the thermoelectric figure of merit  $ZT$ , i.e.  $ZT = \alpha^2 \sigma T / (\kappa_e + \kappa_l)$ , (where  $\alpha$  is Seebeck coefficient,  $\sigma$  is electrical conductivity,  $\kappa_e$  and  $\kappa_l$  are the electrical and lattice components of thermal conductivity) [33]. The improvement in electrical conductivity and defects created due to the incorporation of  $Sr^{2+}$  (reduces thermal conductivity by acting as photon scattering centres) can further lead to tuning of thermoelectric figure of merit ( $ZT$ ) thereby making this composition a potential multifunctional oxide.

The aim of this study is to understand the effect of synthesis route on the structural and optical properties of Sr doped ZnO ( $Zn_{1-x}Sr_xO$  with  $x=0$  to  $0.04$ ) (SZO). The nanoparticles were synthesised by auto combustion, citrate gel method and coprecipitation method. The structural characteristics were studied using the x-ray diffraction technique and optical characteristics using a uv visible spectroscopic technique. Such a study also enabled us to identify the right synthesis route for the preparation of Sr doped ZnO for potential applications.

### 2. Experimental

The nanocrystalline Sr-doped ZnO (SZO) ( $Zn_{1-x}Sr_xO$  with  $x=0$  to  $0.04$ ) was synthesised by three different techniques viz.

\*E-mail address: Shekhar.bhame@sitpune.edu.in

ISSN: 1791-2377 © 2021 School of Science, IHU. All rights reserved.

doi:10.25103/jestr.146.14

auto combustion, citrate gel and coprecipitation techniques. The metal nitrates  $\text{Sr}(\text{NO}_3)_2$  and  $\text{Zn}(\text{NO}_3)_2 \cdot 6\text{H}_2\text{O}$  along with the fuel for auto combustion  $\text{NH}_2\text{CH}_2\text{COOH}$ , chelating agent  $\text{C}_6\text{H}_8\text{O}_7$  for citrate gel method and  $\text{NaOH}$  as precipitating agent in the coprecipitation method was also used.

**2.1. Auto combustion Method (AC)**

In this method, stoichiometric amount of metal nitrates were dissolved completely in distilled water. Glycine nitrate was used as the fuel to ignite the process. Hence glycine nitrate was then added to the mixture after dissolving completely in distilled water. This mixture was set on a hot plate whereby the excess water gets evaporated and forms xerogel that auto combusts to give the nano powder after 2 hours on the hotplate. This nano powder was then annealed at  $600^\circ\text{C}$  for 6 hours followed by fine grinding and characterization.

**2.2. Citrate Gel method (CG)**

In a typical method, the stoichiometric amount of metal nitrates were dissolved in distilled water. Appropriate amount of citric acid was also dissolved in distilled water separately and was mixed with the initial metal nitrate mixture in a crystallizing dish. This dish was kept on a hot plate set at  $100^\circ\text{C}$  until all the excess water in the crystallizing dish evaporates and a xerogel formation takes place. Later, the dish was kept in a hot air oven set at  $100^\circ\text{C}$ . The white residue formed after 12 hours was crushed and annealed at  $600^\circ\text{C}$  for 6 hours followed by characterization.

**2.3. Co-precipitation Method (CP)**

In a co-precipitation method, the stoichiometric amount of metal nitrates were dissolved in distilled water. 5%  $\text{NaOH}$  was added dropwise to precipitate out the metal hydroxides under continues magnetic stirring. The formed precipitates were washed several times and centrifuged until its pH turned neutral. The precipitate was then dried in a hot air oven at  $100^\circ\text{C}$  for 24 hours followed by annealing at  $600^\circ\text{C}$  for 6 hours followed by fine grinding and characterization.

**3. Results and Discussion**

**3.1. X-Ray Diffraction (XRD)**

All the synthesised materials were characterized by room temperature x-ray diffraction (XRD) method to understand the structural properties as shown in Figure 1A-C. All the diffraction results resembled a hexagonal wurtzite like structure of  $\text{ZnO}$  that belong to a space group of P63mc in the Hermann–Mauguin notation with a space group number of 186 (JCPDS # 36–1451) [34]. On a closer analysis of the peaks, it was seen that while AC and CG methods exhibited additional reflections with intensities less than 4%, the additional reflections from coprecipitation was more than 80% with respect to the most intense (101) peak. The additional reflections seen in AC and CG was found to be due to the formation of  $\text{SrCO}_3$  [35], while the additional reflection in CP (at  $2\theta$  at 29.6) was due to  $\text{SrO}$  formation [36].

The variation of cell parameters was unique for all the three methods. While the cell parameters were found to be less than the pristine  $\text{ZnO}$  for AC derived materials on doping from 1 to 3% (Figure 2A), it was found to increase with doping for the CG method from 0 to 4% (Figure 2C). CP derived samples exhibited variation in a tight range from 1 to 3% and resembled an overall ‘M’ shaped curve (Figure 2E). However, it has to be noted that the cell parameters corresponding to 4% doped samples in both the cases (AC and

CP) lay close to the pristine sample with similar trend seen for volume as well.

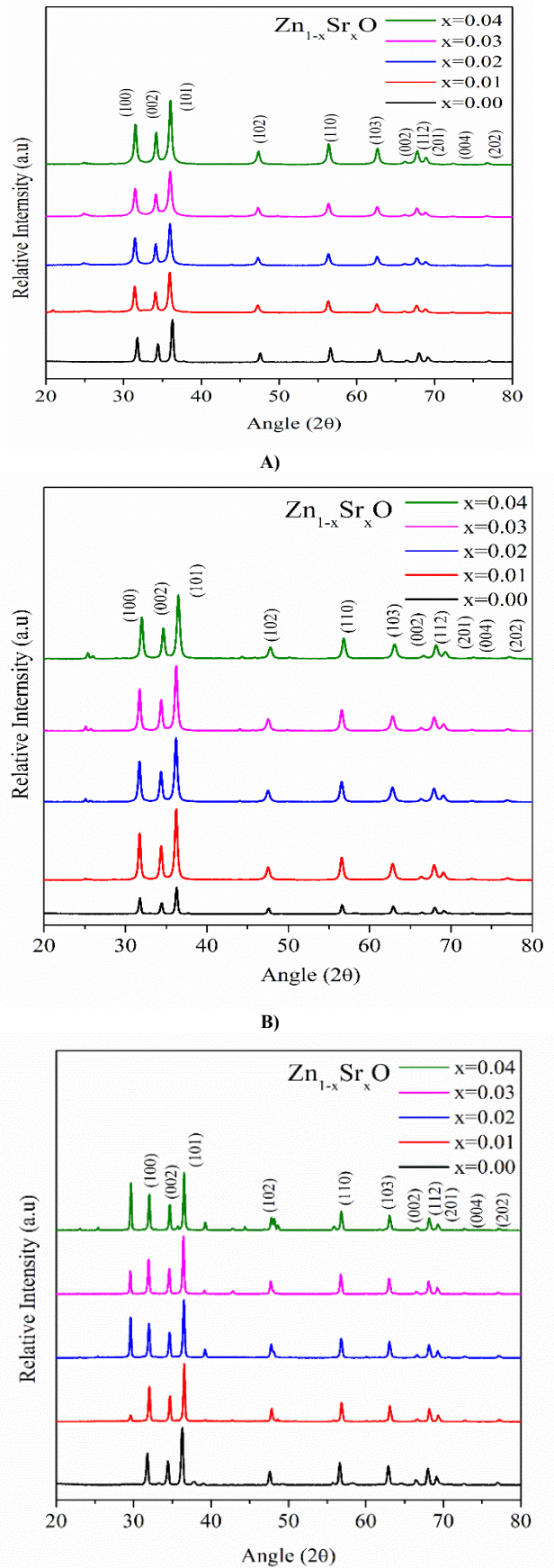


**Fig. 1. A)** Room temperature XRD of SZO series by AC, **B)** Room temperature XRD of SZO series by CG and **C)** Room temperature XRD of SZO series by CP

According to Vegard's law, the contraction in cell parameters 'a' and 'c' or volume on doping of a higher ionic radii element implies a substitutional doping and expansion of cell parameters implies interstitial doping [45]. Applying this theory on the results indicates that:

- i. Interstitial doping takes place up to 2% in the AC followed by substitutional doping.
- ii. Substitutional doping continues to dominate in CG throughout the series.
- iii. Substitutional doping takes place up to 3% followed by interstitial doping in the 4% doped sample.

The bond length (*L*) was seen to be in par with the cell volume for all the methods (Table 1, 2 and 3). The variation of lattice cell parameter was not found to be following a particular trend in the case of AC and CP methods. One of the reasons for such a behaviour could be assigned to the disordered doping of Sr in the host matrix [46]. Results show that *c/a* ratio increases with doping in CG and CP methods (Figure 2C, E) across varying concentration of the dopant. However, a striking dissimilarity was seen in the case of AC derived samples after 1% doping. The crystallite size was seen to be less than the pristine sample in all the methods. Only the 1% doped sample derived by CP showed a minor deviation from this trend (Figure 2F). The reason for *S* and  $\epsilon$  to increase on doping is unconcealed as the ionic radii is extremely large (1.18 Å) than the ions in the host matrix (0.74 Å for Zn<sup>2+</sup>) [47] leading to crystal imperfections and distortions. Apart from the fact that *S* and  $\epsilon$  values varied in

similar trend, all the samples exhibited an inverse relationship of crystallite size with the lattice dislocation and strain. i.e., when the crystallite size increased from one doping level to other, the *S* and  $\epsilon$  values decreased and vice versa. This is because, the particle growth is inhibited by strain in the matrix leading to reduction in crystallite size as seen in all the methods [48].

On comparing the lattice dislocation and strain values of both the methods, it was seen that the samples derived from AC exhibited high lattice dislocation density and strain than the CP samples. Such a behaviour can be explained based on the XRD patterns. It was seen that the CP derived samples exhibited additional reflections corresponding to impurity phases while it was absent in the AC derived. It means that there is a better incorporation of Sr ions in the ZnO lattice for the AC than CP, hence leading to the dislocation and strain since the ionic radii is higher than the Zn ions. The formation of such lattice dislocations and defects can be made use as the source for phonon scattering on using these materials for thermoelectric applications.

### 3.2. UV-Visible Spectroscopy

UV-Visible spectroscopic studies were carried out to study the optical properties of all the synthesised materials (Figure 3A, 3B and 3C). Interesting observations were made for all the methods and the variation of absorption characteristics were evaluated.

**Table 1.** Various structural parameters associated with SZO synthesised by auto combustion method.

Structural parameters of SZO by auto combustion								
x in Zn <sub>1-x</sub> Sr <sub>x</sub> O	a (Å)	c (Å)	c/a	V (Å <sup>3</sup> )	D (nm)	L (Å)	S	ε
0.00	3.2456	5.1985	1.601707	47.42405	18.542	1.975071	0.03783	0.036934
0.01	3.2442	5.1978	1.602182	47.37677	12.3255	1.974404	0.098916	0.0564
0.02	3.2432	5.1955	1.601967	47.32662	12.685	1.973712	0.083507	0.054139
0.03	3.2452	5.1982	1.601812	47.40963	10.747	1.974869	0.109131	0.063762
0.04	3.2456	5.1985	1.601707	47.42405	11.573	1.975071	0.101998	0.056136

**Table 2.** Various structural parameters associated with SZO synthesised by citrate gel method.

Structural parameters of SZO by citrate gel								
x in Zn <sub>1-x</sub> Sr <sub>x</sub> O	a (Å)	c (Å)	c/a	V (Å <sup>3</sup> )	D (nm)	L (Å)	S	ε
0.00	3.2459	5.1987	1.601621	47.43465	17.865	1.97522	0.037438	0.037455
0.01	3.2466	5.2026	1.602476	47.49071	11.911	1.97598	0.100101	0.056636
0.02	3.2468	5.2027	1.602409	47.49747	12.006	1.976075	0.09517	0.058581
0.03	3.2467	5.2028	1.602489	47.49546	13.639	1.976045	0.077935	0.050015
0.04	3.2491	5.2068	1.602536	47.60227	11.168	1.977525	0.116634	0.060693

**Table 3.** Various structural parameters associated with SZO synthesised by coprecipitation method.

x in Zn <sub>1-x</sub> Sr <sub>x</sub> O	a (Å)	c (Å)	c/a	V (Å <sup>3</sup> )	D (nm)	L (Å)	S	ε
0.00	3.2455	5.199	1.60191	47.42569	22.893	1.97509	0.021154	0.029992
0.01	3.2512	5.209	1.602178	47.68397	31.959	1.978663	0.01541	0.022784
0.02	3.2502	5.2077	1.602271	47.64274	19.58	1.97809	0.037965	0.034589
0.03	3.2505	5.2085	1.602369	47.65886	22.107	1.978311	0.025798	0.030285
0.04	3.2437	5.1987	1.602707	47.37037	14.607	1.974305	0.108813	0.052234

The absorption spectrum revealed that, all the materials exhibited near band edge emission close to 360 nm which is a typical for ZnO based materials and the absorption edge

shifts to lower wavelength as the concentration of dopant increases. Unlike some of the previous reports wherein a red shift in absorption edge on Sr doping was seen resulting in

absorption in the visible region [49], our results indicate a blue shift. While we observed excellent absorption in the visible light region within 400 to 700 nm in addition to the typical UV absorption for the AC method, no reference to intense absorption after 400 nm for Sr doped ZnO was available. This behaviour can be attributed to the “charge transfer between ZnO valence or conduction band and the Sr 2*p* ion 5*s* level” [49]. We observed intense absorption in the visible light in the case of AC method and 3% doped sample in CG method. However, CP showed no absorption in the visible light range. It is indeed interesting to see that 3% doped sample in AC and CG methods are showing the highest

visible light activity. The absorption in the visible range was found to be within 700 nm. A number of reasons could be assigned to explain such an absorbance pattern. Firstly, since Sr is a high ionic radii element (1.18 Å), on doping it in the ZnO matrix with relatively lower ionic radii (0.74Å) can lead to structural defects as seen from the XRD studies. Such defects can lead to intermediate bands between the valence and conduction bands leading to visible light absorption [49; 50]. Such an absorption in the visible light range could make this material, especially the SZO synthesised by AC an apt photocatalyst for dye degradation applications.

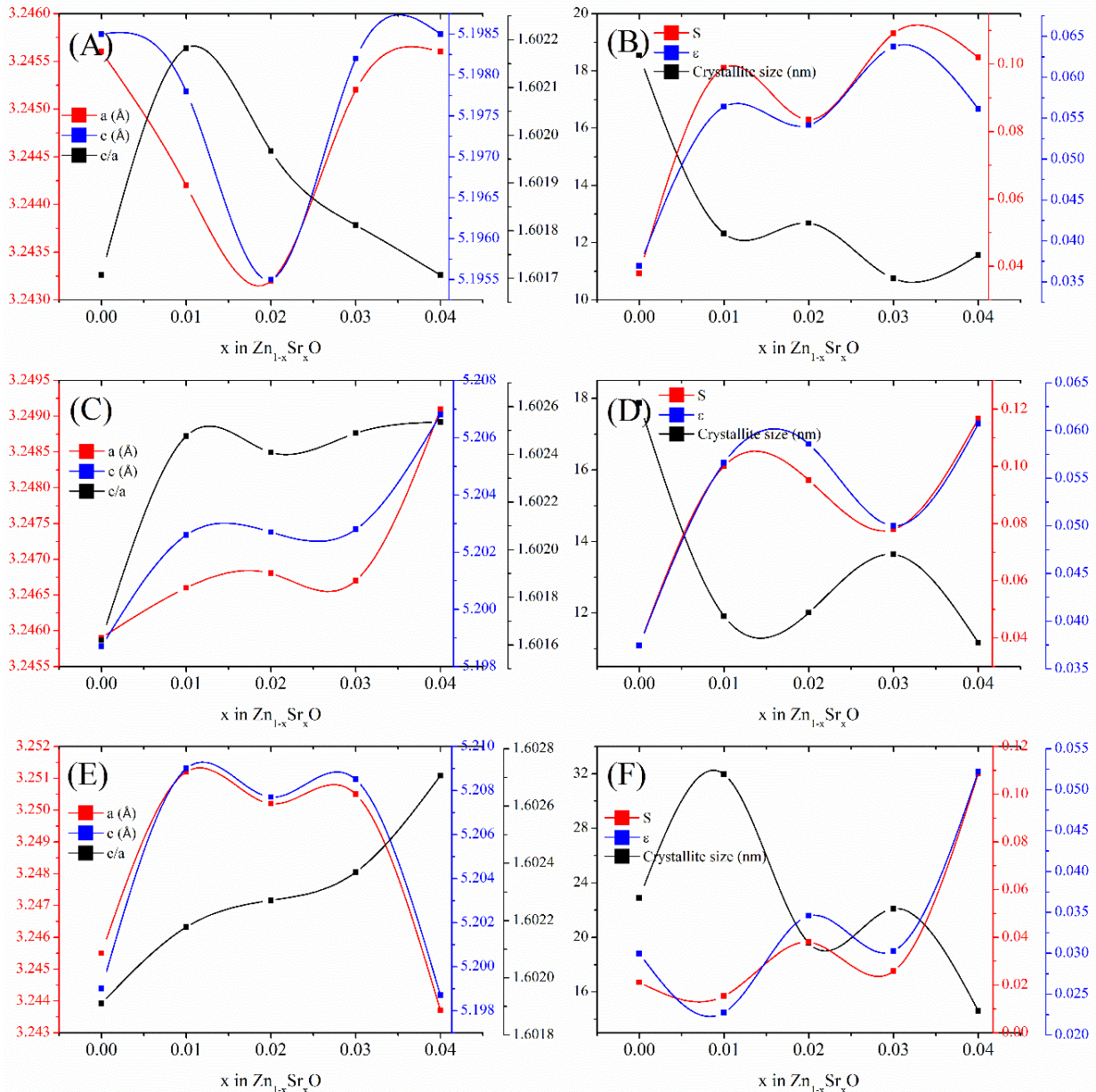


Fig. 2. Variation of lattice cell parameters, crystallite size, dislocation density and strain with respect to dopant concentration in AC method (A,B), CG method (C,D) and CP method (E,F)

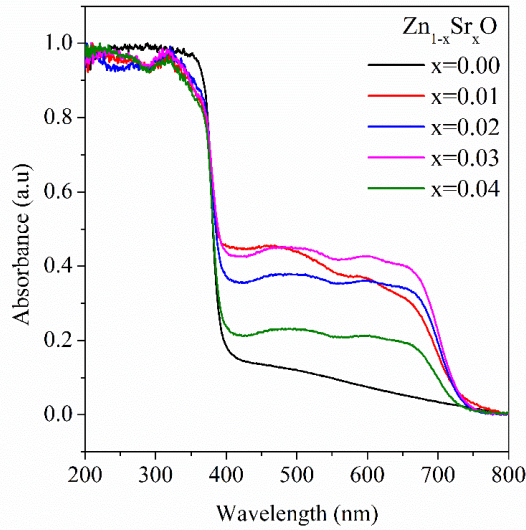


Fig. 3A. Absorption spectrum of SZO series by AC

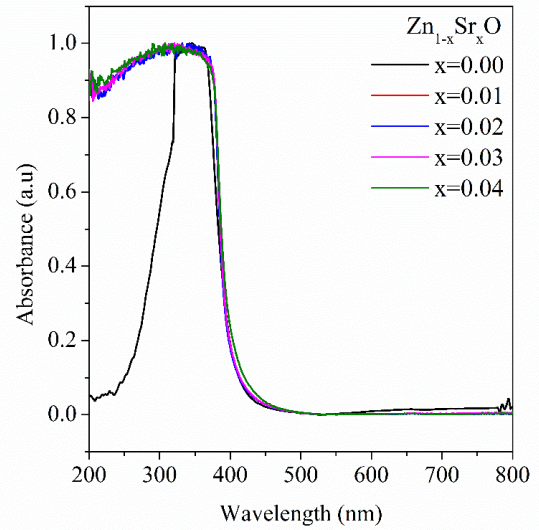


Fig. 3C. Absorption spectrum of SZO series by CP

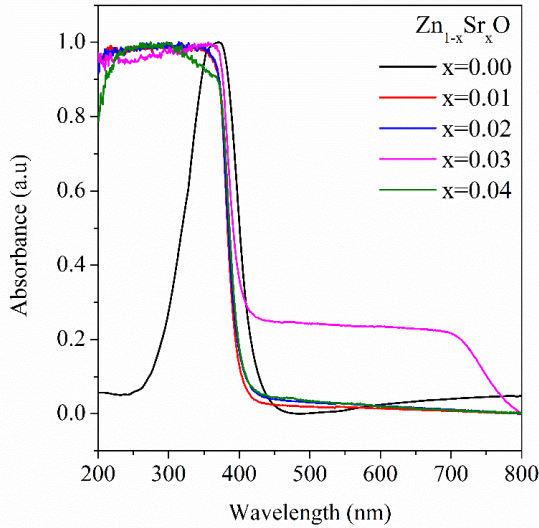
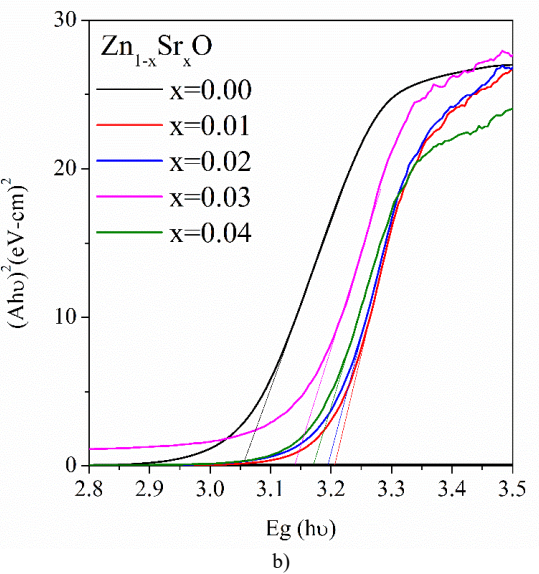
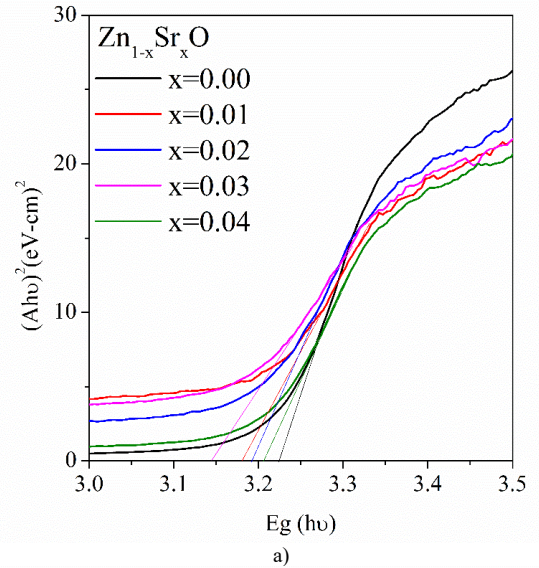


Fig. 3B. Absorption spectrum of SZO series by CG



Tau<sup>c</sup> plot method was followed to derive the band gap of all the materials. The Tau<sup>c</sup> method is defined by the equation 5:

$$ahv = (hv - E_g)^n \quad (5)$$

Where  $\alpha$  (absorption coefficient) =  $2.303A/t$ ,  $A$  and  $t$  is the absorbance and thickness of cuvette,  $h$  is planks constant,  $\nu$  is the photon frequency,  $E_g$  is the optical bandgap and  $n = 1/2, 2, 3/2$  and  $3$  for direct allowed, indirect allowed, direct forbidden and indirect forbidden transitions respectively.

Extrapolating leaner portion of  $(Ahv)^2$  on the x-axis in a plot of  $(Ahv)^2$  vs  $h\nu$  gives the optical bandgap [51]. Tau<sup>c</sup> plot for all the samples derived from various methods are shown in the figure 4A-C.

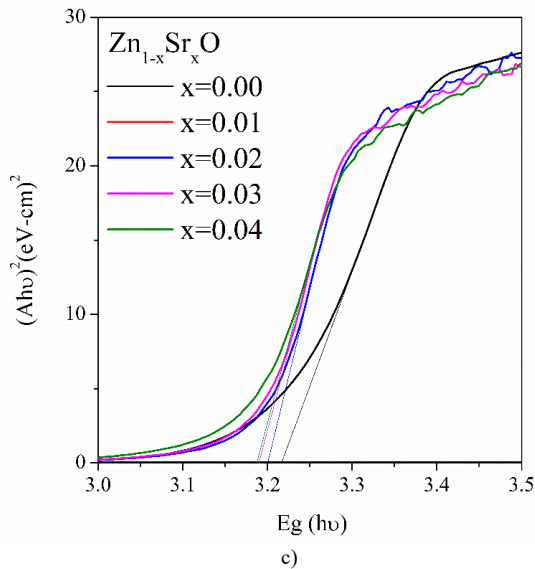


Fig. 4a). Tau<sup>2</sup>c plot of SZO series by AC, b) Tau<sup>2</sup>c plot of SZO series by CG and c) Tau<sup>2</sup>c plot of SZO series by CP

On comparing the Figure 4A-C it was seen that, even the pristine samples exhibited varying bandgap as a consequence of the synthesis technique followed. On looking at the variation of bandgap only for pristine ZnO across all the methods, CG method derived ZnO exhibit the least bandgap of 3.05 eV. This result gives an insight into the engineering of bandgap solely by tuning the synthesis without any dopant. For the doped samples, while the bandgap decreased in the case of AC method on doping (Figure 4A), it increased for the CG method (Figure 4B) and remained almost in the same range for CP (Figure 4C) with a sharp deviation for only 3% doped sample. Since the crystallite size distribution was almost in the same range for AC and CG methods (Table 1), a number of reasons such as: defect states in between the valence band maximum and conduction band minimum, strain and lattice distortions induced due to doping might have led to such a variation in bandgap [52]. However, the increase in bandgap as seen for the case of CG derived samples can be attributed to the Burstein Moss (BM) effect [53]. Calculations suggest that, increase in the BM shift is a consequence of increase in electron density as understood from the theory [54].

This could be beneficial for thermoelectric applications as electron density and electronic conductivity are directly related. On comparing the AC and CG methods to CP method, the variation in crystallite size is not in a single range like in the case of AC and CG. A common trend that was observed in AC method is the reduction of bandgap with the addition of Sr. Such a variation might be due to the *p-d* spin exchange interactions and introduction of defect states near the conduction band as well explained in the references [45; 55; 56]. It has been proven theoretically that Zn-3*d* and O-2*p* contributes to the higher valence band; Zn-4*s* and O-2*p* contributes to the lower conduction band in ZnO. On Sr doping, additional Sr-3*d* levels are introduced in the conduction band [57]. Such an introduction of additional level can lead to higher mobility of carriers. Such a feature would enable ZnO to be tuned as a thermoelectric application as carrier mobility and electrical conductivity is directly proportional ( $\sigma = ne\mu$  where  $\sigma$ ,  $n$ ,  $e$  and  $\mu$  is the electrical conductivity, carrier concentration, charge of electron and carrier mobility respectively) [58]. For a matter of evidence, reference [32] has reported improvement in electrical

conductivity on doping Sr in ZnO. While it becomes difficult to understand the bandgap variations in the CP method as any appreciable change was seen only for the 3% doped sample, excellent correlation between the bandgap and crystallite size was seen in the CG method (Figure 5B). Such a correlation arises as a result of the quantum confinement effect defined by the equation 6:

$$E_{gap}^{NP} = \frac{hc}{\lambda} = E_{gap}^{Bulk} + \frac{h^2}{8r^2} \left( \frac{1}{m_e^*} + \frac{1}{m_h^*} \right) - \frac{1.8e^2}{4\pi\epsilon_0\epsilon_r} \quad (6)$$

where  $E_{gap}^{NP}$ ,  $E_{gap}^{Bulk}$ ,  $h$ ,  $c$ ,  $\lambda$ ,  $r$ ,  $m_e^*$ ,  $m_h^*$ ,  $\epsilon_0$  and  $\epsilon_r$  are energy bandgap of nanomaterial, bulk material, planks constant, velocity of light, wavelength of light used, radius of the particles, effective mass of electron and hole, dielectric constant of material and that of free space respectively [59]. Hence an inverse relation between the bandgap and particle size can be seen from the equation above which is also reflected in our results (Figure 5B). The change in bandgap and crystallite size however was found to be varying in a similar manner for the AC derived samples (Figure 5A). Such variations are well explained in reference [60] and the narrowing of bandgap is because of the many body interactions [61]. Such totally opposite relations seen in AC and CG methods are purely because of the influence of synthesis route on the structural and optical properties of the material under study.

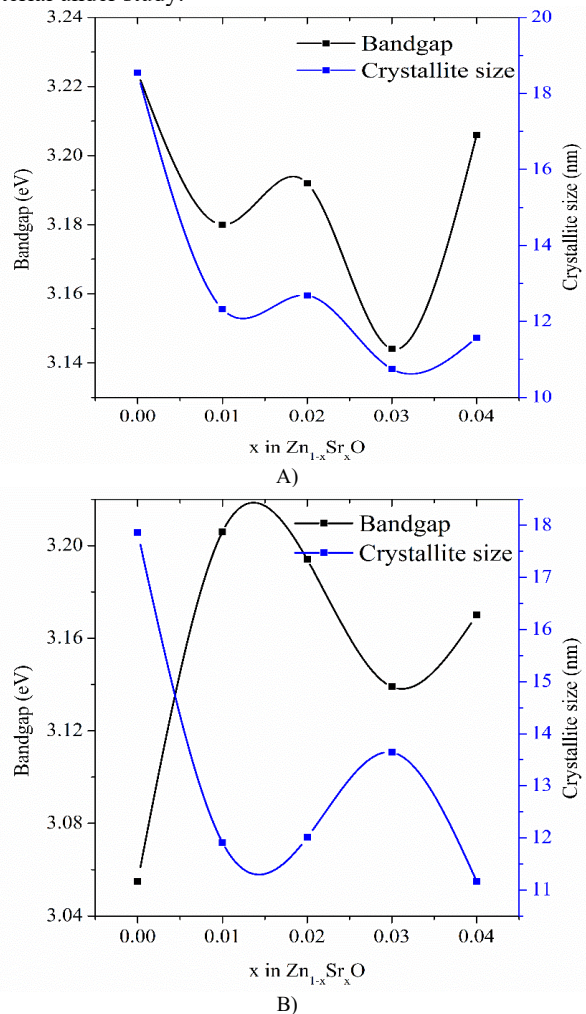


Fig. 5A. Variation of bandgap and crystallite size with variation in dopant concentration synthesised by AC method and B. Variation of bandgap and crystallite size with variation in dopant concentration synthesised by CG method.

#### 4. Conclusions

Sr doped ZnO ( $Zn_{1-x}Sr_xO$  with  $x=0, 0.01, 0.02, 0.03$  and  $0.04$ ) was synthesised by three different methods viz. auto combustion, citrate gel and coprecipitation methods. XRD revealed that auto combustion and citrate gel methods led to additional reflections less than 4% while coprecipitation derived samples exhibited impurity reflections with intensity more than 80%. Hence auto combustion and citrate gel methods have been identified as best suited methods for the synthesis of Sr doped ZnO. One of the primary differences between all these methods is the introduction of thermal treatment at the time of nucleation. Since the characteristics of the synthesised materials depends on the growth environment, as per our observation, presence of temperature more than  $80^\circ\text{C}$  is essential at the time of nucleation for better incorporation of Sr in the ZnO matrix. The incorporation of such a high ionic radii element like Sr also leads to high strain in the crystal and dislocation density leading to number of defects. In addition to the absorption in UV region, auto

combustion method derived samples exhibited promising visible light absorption. Such absorption in the visible region makes auto combustion derived SZO a potential candidate for photocatalytic dye degradation. At the same time, SZO might also be a potential thermoelectric candidate as the defects induced in the crystal lattice can lead to phonon scattering thereby reducing the thermal conductivity while the addition of Sr-3d levels to conduction band would be helpful in increasing the carrier mobility and electrical conductivity leading to better  $ZT$ .

#### Acknowledgements

One of the author Mr. Rishi Prasad would like to thank Symbiosis International (Deemed University) for the award of research fellowship.

This is an Open Access article distributed under the terms of the Creative Commons Attribution License.



#### References

- Ü. Özgür, Y. I. Alivov, C. Liu, A. Teke, M. Reshchikov, S. Doğan, V. Avrutin, S.-J. Cho, Morkoç, *J. Appl. Phys.* **2005**, *98*, 11.
- R. Prasad, P. S. Walke, S. D. Bhamre, *Materials Research Express.* **2019**, *6*, 1150b1158.
- V. A. Coleman, C. Jagadish, "Basic properties and applications of ZnO," *Zinc oxide bulk, thin films and nanostructures*, Elsevier **2006**, p. 1-20.
- S. Chaudhary, A. Umar, K. Bhasin, S. Baskoutas, *Materials.* **2018**, *11*, 287.
- L.-E. Shi, Z.-H. Li, W. Zheng, Y.-F. Zhao, Y.-F. Jin, Z.-X. Tang, *Food Additives & Contaminants: Part A.* **2014**, *31*, 173-186.
- T.-H. Moon, M.-C. Jeong, W. Lee, J.-M. Myoung, *Appl. Surf. Sci.* **2005**, *240*, 280-285.
- M. Behnajady, N. Modirshahla, R. Hamzavi, *J. Hazard. Mater.* **2006**, *133*, 226-232.
- Y. Zhang, Y. Yang, J. Zhao, R. Tan, W. Wang, P. Cui, W. Song, *Journal of Materials Science.* **2011**, *46*, 774-780.
- Y. S. Sonawane, K. Kanade, B. Kale, R. Aiyyer, *Mater. Res. Bull.* **2008**, *43*, 2719-2726.
- S. Rasouli, S. J. Moeen, *J. Alloys Compd.* **2011**, *509*, 1915-1919.
- V. C. Srivastava, *Industrial & Engineering Chemistry Research.* **2013**, *52*, 17790-17799.
- S. Cimitan, S. Albonetti, L. Forni, F. Peri, D. Lazzari, *J. Colloid Interface Sci.* **2009**, *329*, 73-80.
- A. Murali, P. Sarswat, H. Sohn, *Materials today chemistry.* **2019**, *11*, 60-68.
- R. Elilarassi, G. Chandrasekaran, *Optoelectronics letters.* **2010**, *6*, 6-10.
- R. Prasad, S. D. Bhamre, *Materials for Renewable and Sustainable Energy.* **2020**, *9*, 3.
- P. Jood, R. J. Mehta, Y. Zhang, G. Peleckis, X. Wang, R. W. Siegel, T. Borca-Tasciuc, S. X. Dou, G. Ramanath, *Nano Lett.* **2011**, *11*, 4337-4342.
- J. Kennedy, P. P. Murmu, J. Leveneur, V. Williams, R. L. Moody, T. Maity, S. V. Chong, *Journal of Nanoscience and Nanotechnology.* **2018**, *18*, 1384-1387.
- Y. Fujishiro, M. Miyata, M. Awano, K. Maeda, *J. Am. Ceram. Soc.* **2003**, *86*, 2063-2066.
- K. H. Kim, S. H. Shim, K. B. Shim, K. Niihara, J. Hojo, *J. Am. Ceram. Soc.* **2005**, *88*, 628-632.
- P. Zhang, R. Hong, Q. Chen, W. Feng, *Powder Technol.* **2014**, *253*, 360-367.
- M. Ahmad, E. Ahmed, Y. Zhang, N. Khalid, J. Xu, M. Ullah, Z. Hong, *Current Applied Physics.* **2013**, *13*, 697-704.
- J.-D. Wang, J.-K. Liu, Q. Tong, Y. Lu, X.-H. Yang, *Industrial & Engineering Chemistry Research.* **2014**, *53*, 2229-2237.
- M. J. Haque, M. M. Bellah, M. R. Hassan, S. Rahman, *Nano Express.* **2020**, *1*, 010007.
- A. Kołodziejczak-Radzimska, T. Jesionowski, *Materials.* **2014**, *7*, 2833-2881.
- G. Mazitova, K. Kienskaya, D. Ivanova, I. Belova, I. Butorova, M. Sardushkin, *Review Journal of Chemistry.* **2019**, *9*, 127-152.
- S. Brintha, M. Ajitha, *IOSR J. Appl. Chem.* **2015**, *8*, 66-72.
- R. Saha, S. Karthik, K. S. Balu, R. Suriyaprabha, P. Siva, V. Rajendran, *Mater. Chem. Phys.* **2018**, *209*, 208-216.
- Y. Han, D. Kim, G. Hwang, B. Lee, I. Eom, P. J. Kim, M. Tong, H. Kim, *Colloids and Surfaces A: Physicochemical and Engineering Aspects.* **2014**, *451*, 7-15.
- R. M. Sheetz, I. Ponomareva, E. Richter, A. N. Andriotis, M. Menon, *Physical Review B.* **2009**, *80*, 195314.
- M. Kavitha, K. Jinesh, R. Philip, P. Popinath, H. John, *PCCP.* **2014**, *16*, 25093-25100.
- J. Wang, Z. Wang, B. Huang, Y. Ma, Y. Liu, X. Qin, X. Zhang, Y. Dai, *ACS applied materials & interfaces.* **2012**, *4*, 4024-4030.
- T. Vijayan, R. Chandramohan, S. Valanarasu, J. Thirumalai, S. Subramanian, *Journal of Materials Science.* **2008**, *43*, 1776-1782.
- G. J. Snyder, E. S. Toberer, "Complex thermoelectric materials," *Materials for sustainable energy: a collection of peer-reviewed research and review articles from Nature Publishing Group*, World Scientific **2011**, p. 101-110.
- Y. Chen, R. Yu, Q. Shi, J. Qin, F. Zheng, *Mater. Lett.* **2007**, *61*, 4438-4441.
- N. N. Kumaran, K. Muraleedharan, *Journal of water process engineering.* **2017**, *17*, 264-270.
- F. Granados-Correa, J. Bonifacio-Martínez, *Materials Science-Poland.* **2014**, *32*, 682-687.
- J. Xu, Q. Pan, Z. Tian, *Sensors and Actuators B: Chemical.* **2000**, *66*, 277-279.
- S. Bhamre, P. Joy, *Sensors and Actuators A: Physical.* **2007**, *137*, 256-261.
- L. A. Chick, L. Pederson, G. Maupin, J. Bates, L. Thomas, G. Exarhos, *Mater. Lett.* **1990**, *10*, 6-12.
- PowderCell, 2.4, Berlin, <https://powdercell-for-windows.software.informer.com/versions/>, Berlin.
- M. Sathya, K. Pushpanathan, *Appl. Surf. Sci.* **2018**, *449*, 346-357.
- A. Pourrahimi, D. Liu, V. Ström, M. S. Hedenqvist, R. T. Olsson, U. W. Gedde, *Journal of Materials Chemistry A.* **2015**, *3*, 17190-17200.
- B. R. Kumar, B. Hymavathi, *Advances in Natural Sciences: Nanoscience and Nanotechnology.* **2018**, *9*, 035018.
- V. Mote, Y. Purushotham, B. Dole, *Journal of Theoretical and Applied Physics.* **2012**, *6*, 6.

45. M. Shkir, B. M. Al-Shehri, M. Pachamuthu, A. Khan, K. V. Chandekar, S. AlFaify, M. S. Hamdy, *Colloids and Surfaces A: Physicochemical and Engineering Aspects*. **2020**, 587, 124340.
46. N. M. Basith, J. J. Vijaya, L. J. Kennedy, M. Bououdina, *Mater. Sci. Semicond. Process.* **2014**, 17, 110-118.
47. R. D. Shannon, *Acta crystallographica section A: crystal physics, diffraction, theoretical and general crystallography*. **1976**, 32, 751-767.
48. T. Srivastava, G. Bajpai, G. Rathore, P. Mishra, S. W. Liu, S. Biring, S. Sen, *arXiv preprint arXiv:1803.06656*. **2018**.
49. D. Li, J.-F. Huang, L.-Y. Cao, L. Jia-Yin, H.-B. OuYang, C.-Y. Yao, *Ceram. Int.* **2014**, 40, 2647-2653.
50. L. Xu, S. Xiao, C. Zhang, G. Zheng, J. Su, L. Zhao, J. Wang, *Mater. Chem. Phys.* **2014**, 148, 720-726.
51. T. P. Rao, M. S. Kumar, S. A. Angayarkanni, M. Ashok, *J. Alloys Compd.* **2009**, 485, 413-417.
52. S. Kumar, S. Basu, B. Rana, A. Barman, S. Chatterjee, S. Jha, D. Bhattacharyya, N. Sahoo, A. K. Ghosh, *Journal of Materials Chemistry C*. **2014**, 2, 481-495.
53. E. Burstein, *Physical Review*. **1954**, 93, 632.
54. B. E. Sernelius, K. F. Berggren, Z. C. Jin, I. Hamberg, C. G. Granqvist, *Physical Review B*. **1988**, 37, 10244-10248.
55. K. P. Raj, K. Sadaiyandi, A. Kennedy, R. Thamizselvi, *Mater. Chem. Phys.* **2016**, 183, 24-36.
56. R. Udayabhaskar, B. Karthikeyan, *J. Appl. Phys.* **2014**, 116, 094310.
57. A. Mahmood, F. Tezcan, G. Karadaş, F. Karadağ, *J. Appl. Phys.* **2017**, 122, 113102.
58. M. Markov, X. Hu, H.-C. Liu, N. Liu, S. J. Poon, K. Esfarjani, M. Zebarjadi, *Scientific reports*. **2018**, 8, 1-10.
59. M. El-Hagary, E. Shaaban, S. Moustafa, G. Gad, *Materials Research Express*. **2018**, 6, 015030.
60. S. Benramache, O. Belahssen, A. Guettaf, A. Arif, *Journal of Semiconductors*. **2014**, 35, 042001.
61. A. Talin, K. Dean, J. Jaskie, "Solid-State Electron," in (2001)